

ARTICLE OPEN



Simultaneous enhancement in electrical conductivity and Seebeck coefficient by single- to double-valley transition in a Dirac-like band

Yu Dai¹, Wenjiang Zhou¹, Hyun-Jung Kim², Qichen Song³, Xin Qian¹, Te-Huan Liu¹ and Ronggui Yang¹

SnTe possesses a single- to double-valley transition in the conduction band minimum when a compressive strain is applied. Through a tight-binding analysis, it is shown that the variation of the band structure is attributed to the strain-induced delocalization of both the Sn-5s orbitals and Te-5p orbitals with different angular momenta. This effect can largely increase the electron density of states near the band edge and thus keep the Fermi level of the compressed SnTe closer to it, where the electrons have lower scattering rates. The strain-induced double valleys lead to simultaneous increases in the electrical conductivity and the Seebeck coefficient and thereby nearly four times the enhancement of the power factor at the doping concentration of $5 \times 10^{19} \text{ cm}^{-3}$. This work suggests a feasible concept that can be employed to promote the power factor of a Dirac semiconductor via manipulating the valley degeneracy in the conduction band minimum.

npj Computational Materials (2022)8:234; <https://doi.org/10.1038/s41524-022-00927-z>

INTRODUCTION

In the past few decades, many great strides have been made in thermoelectric materials and technology to improve the capability to convert waste heat into electric power or to arrive at high-performance solid-state refrigeration^{1–7}. To evaluate the conversion efficiency of thermoelectric materials, a dimensionless figure of merit, $zT = \sigma S^2 T / (\kappa_{\text{ph}} + \kappa_{\text{e}})$, has been employed, in which σ is the electrical conductivity, S is the Seebeck coefficient, κ_{ph} and κ_{e} are the phonon and electronic thermal conductivities, respectively, and T is the absolute temperature. A good thermoelectric material is expected to have a high power factor as well as a low thermal conductivity. In practice, the material properties (σ , S , and $\kappa_{\text{ph}} + \kappa_{\text{e}}$) need to be balanced against each other, and sophisticated techniques regarding material design must be involved⁸, such as nanostructured materials^{5,9–11}, all-scale hierarchical architectures^{12,13}, band engineering^{14,15}, resonant impurity doping and alloying^{16–19}, and strain engineering²⁰. Other heuristic methods have been discussed in previous reviews^{21–23}.

In recent years, SnTe rises to a prominent position among semiconductors not only because it is a topological crystalline insulator^{24,25} but also because it has great potential for use in low-cost, non-toxic thermoelectric devices²². The incorporation of heavy elements with strong spin-orbit coupling (SOC) profoundly affects the band structure of GeTe, SnTe, and PbTe²⁶. The presence of s - p hybridization at the L point in rock-salt crystals can elevate the anion's p orbital to form a conduction band, leading to so-called band inversion²⁶. Among the three group-IV tellurides, the inverted bands are found only in SnTe, which is, therefore, a topological crystalline insulator, while the other group-IV tellurides are normal semiconductors. This feature differentiates SnTe as it has a Dirac-like band near the edges and a continuously tunable bandgap with strain²⁷, pressure²⁸, and alloying²⁹. The quasi-linear dispersion is particularly beneficial for nanostructuring degenerate semiconductors because the long-

mean-free-path (MFP) carriers that are detrimental to the total Seebeck coefficient would suffer stronger boundary scattering than the short-MFP carriers³⁰. A recent experiment²⁹ showed that multiple valleys appeared in both the conduction and valence band edges after alloying 25% GeTe and 25% PbTe into SnTe, which induced a $\sim 0.7\%$ internal strain in the crystal and led to the band inversion. These studies revealed the possibility of obtaining higher power factors for SnTe in terms of manipulating the Dirac-like band electronic characteristics.

Many studies have shown that p -type SnTe has an enormous enhancement in the power factor through manipulating the electron band structure, which utilizes its iconic tunable bandgap and band inversion as mentioned^{24,27}. The intrinsic bandgap at the L point can be expanded by alloying with Cd, Mn, Mg, or other metallic atoms^{31–33} and semiconductor compounds³⁴, leading to the convergence of the first and second valence bands and the resulting improvement of the hole Seebeck coefficient. Using two resonant dopants—for example, co-doping with Bi-In³⁵ and Bi-Zn³⁶ is also a common strategy to enhance the power factor of SnTe. These methods usually bring about a changed effective mass, band crossing, and additional channels for phonon scattering, and the synergistic effects can further enhance the peak zT to 1.85 at 823 K³⁷. In addition to controlling the electron transport, the introduction of crystal imperfections^{38,39} and the inducement of soft modes⁴⁰ in SnTe can result in poor thermal conductivity. To date, there have been relatively few studies on n -type SnTe. A previous density-functional theory (DFT) study predicted that n -type SnTe would be a good thermoelectric material⁴¹. Recently, the $\text{Sn}_{0.6}\text{Pb}_{0.4}\text{Te}_{0.98}\text{I}_{0.02}$ compound (with Pb alloying to reduce Sn vacancies and I dopant to increase carrier concentration) has been experimentally found to have a good mid-temperature zT of ~ 0.8 at 573 K⁴². Furthermore, with Pb alloying leading to a topological phase transition, an n -type

¹School of Energy and Power Engineering, Huazhong University of Science and Technology, Wuhan, Hubei 430074, China. ²Peter Grünberg Institut and Institute for Advanced Simulation, Forschungszentrum Jülich and JARA, D-52425 Jülich, Germany. ³Department of Chemistry and Chemical Biology, Harvard University, Cambridge, MA 02138, USA. ✉email: thliu@hust.edu.cn; ronggui@hust.edu.cn

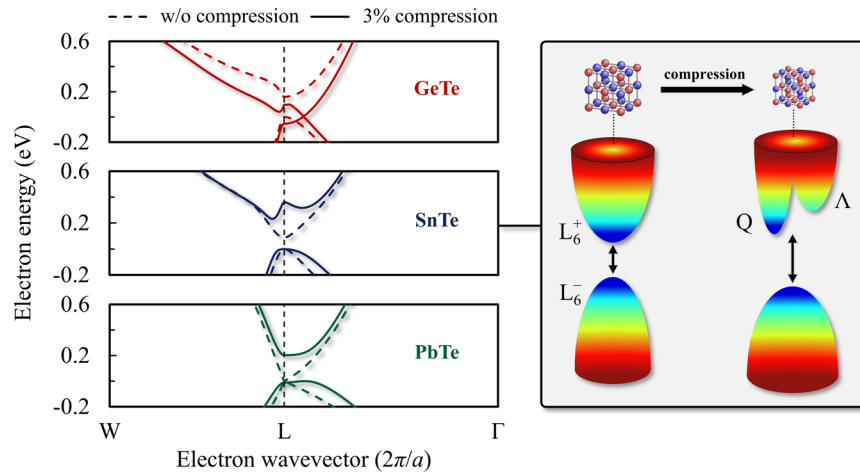


Fig. 1 Evolution of band structures due to different compressive strains. The left plots show the ab initio electron band structures of GeTe (red), SnTe (blue), and PbTe (green). The solid and dashed lines represent the crystal with and without a 3% compressive strain, respectively. The right plot schematically illustrates the transition of the band structure of SnTe after compression. The bottoms of the two new-formed conduction valleys in SnTe are denoted as Q (located at $0.4831\mathbf{b}_1 + 0.5169\mathbf{b}_2 + 0.5000\mathbf{b}_3$ in the direction from the L to W point) and Λ (located at $0.4575\mathbf{b}_1 + 0.4575\mathbf{b}_2 + 0.4575\mathbf{b}_3$ in the direction from the L to Γ point), where \mathbf{b} is the reciprocal lattice vector.

SnTe-Pb-Br crystal can have an average zT of up to ~ 0.58 from room temperature to 823 K⁴³.

In bulk SnTe, a double-valley structure in the conduction band due to a reduced lattice constant has been reported^{27,44}. Intuitively, the transition of the single valley to double valleys affects electron transport; and it is desired to have a quantitative study with mode-by-mode analysis based on ab initio calculations for this effect. Herein, we investigate the origins of the strain-induced double-valley band-structure transition as well as its effect on the electron transport using a tight-binding analysis and ab initio calculations. The compressive strain increases the overlapping of wavefunctions of the 5s electrons between each adjacent Sn site and of the 5p electrons with different orbital angular momenta between each adjacent Te site, which leads to the transition of the conduction band minimum (CBM) from single valley to double valleys. In compressed SnTe, the electron density of states (DOSs) near the band edge is correspondingly increased, thus simultaneously enhancing the electrical conductivity and the Seebeck coefficient compared to the unstrained crystal. It renders the *n*-type SnTe a high-efficiency thermoelectric material with a room-temperature power factor of up to $13.7 \mu\text{W cm}^{-1} \text{K}^{-2}$ at the doping concentration of $5 \times 10^{19} \text{cm}^{-3}$ after a 3% compression.

RESULTS AND DISCUSSION

Figure 1 shows the changes in the electron band structures around the band extrema of the three group-IV telluride compounds GeTe, SnTe, and PbTe when a 3% compressive strain is applied. The evolution of the bandgap with changing lattice constants is provided in Supplementary Fig. 1 in the Supplementary Material. In PbTe, the CBM remains a single valley even if a 3% compressive strain is applied. A slight change in bandgap in GeTe can be observed after the occurrence of topological insulator transition (the energy offset of $L_6^- - L_6^+$ equals zero), which is quite different from those of SnTe and PbTe. In the 3% compressed GeTe, a tiny gap of less than 0.003 eV is reopened where the CBM is majorly contributed by the Ge-4p electrons while the valence band maximum is by Te-5p electrons. This feature shows the compressed GeTe as a semimetal, which could be attributed to the weak *p-p* couplings that refrain from the formation of a significant forbidden zone. On the other hand, the cubic structure is present in the high-temperature phase of GeTe when the temperature is higher than 720 K⁴⁵. In a semimetal at elevated temperatures, electron-hole pairs can transport energy equal to

the sum of the electron and hole's energies⁴⁶. Therefore, bipolar diffusion could bring about a non-negligible contribution to the electronic thermal conductivity in the compressed GeTe in addition to the diffusion of the electrons and holes themselves, which is unfavorable for thermoelectric applications. A distinct change can be observed in the SnTe—the strain increases the bandgap and induces a double-valley splitting near the conduction band edge, forming two new conduction valleys denoted as Q and Λ (right panel of Fig. 1). A more detailed band shape evolution for SnTe with different strains and the corresponding pressure on the crystal are provided in Supplementary Fig. 2 in the Supplementary Material. In the group-IV tellurides, the lone-pair *s* band of cations is allowed to couple with the valence *p* band of the Te atom at the L point while the process is forbidden at the Brillouin zone center²⁶. The *s-p* coupling is particularly strong in the SnTe, pushing the Te-5p electrons to participate in the formation of the lowest unoccupied state. The bandgap will be increased with increasing pressure when the lattice constant is smaller than the topological phase transition point. Furthermore, this effect can be enhanced by applying hydraulic pressure or compressive strains on the crystal, which increases the bandgap and makes the topological state more robust^{24,28}. The shape of the CBM is sensitive to the varying lattice constant, which drastically changes the contribution of the “inverted” 5p electrons at the L_6^+ point⁴⁴. In practice, this can be achieved by applying strain or pressure to SnTe crystals^{27,28} or alloying with other semiconductor compounds²⁹.

To clarify the origins of double-valley transition, the electronic eigenstates of the three characteristic points (L_6^+ , Q, and Λ) are projected onto the (100) plane, and the charge density profiles are displayed in Fig. 2a. Our calculations show that at the L_6^+ point, the contribution of the Te-5p electrons decreases from 58% to 45% after a 3% compression. This leads to the increase of the Sn-5s electrons, which is also reflected by the variation of the charge density around the Sn atoms. The constitutions of the orbitals at the Q and Λ points are more complex, but the contributions of the Sn-5s and Te-5p electrons are both increased as the compressive strain is applied. We perform a tight-binding analysis to further investigate the band structures and atomic orbital contribution. The differences in each matrix element of the crystal Hamiltonian arising from the compression are shown in Fig. 2b. This plot reflects the fact that the Sn-5s electrons become more delocalized (colored with red), which enhances the overlapping of the wavefunctions of the periodic replicas. On the other hand, the

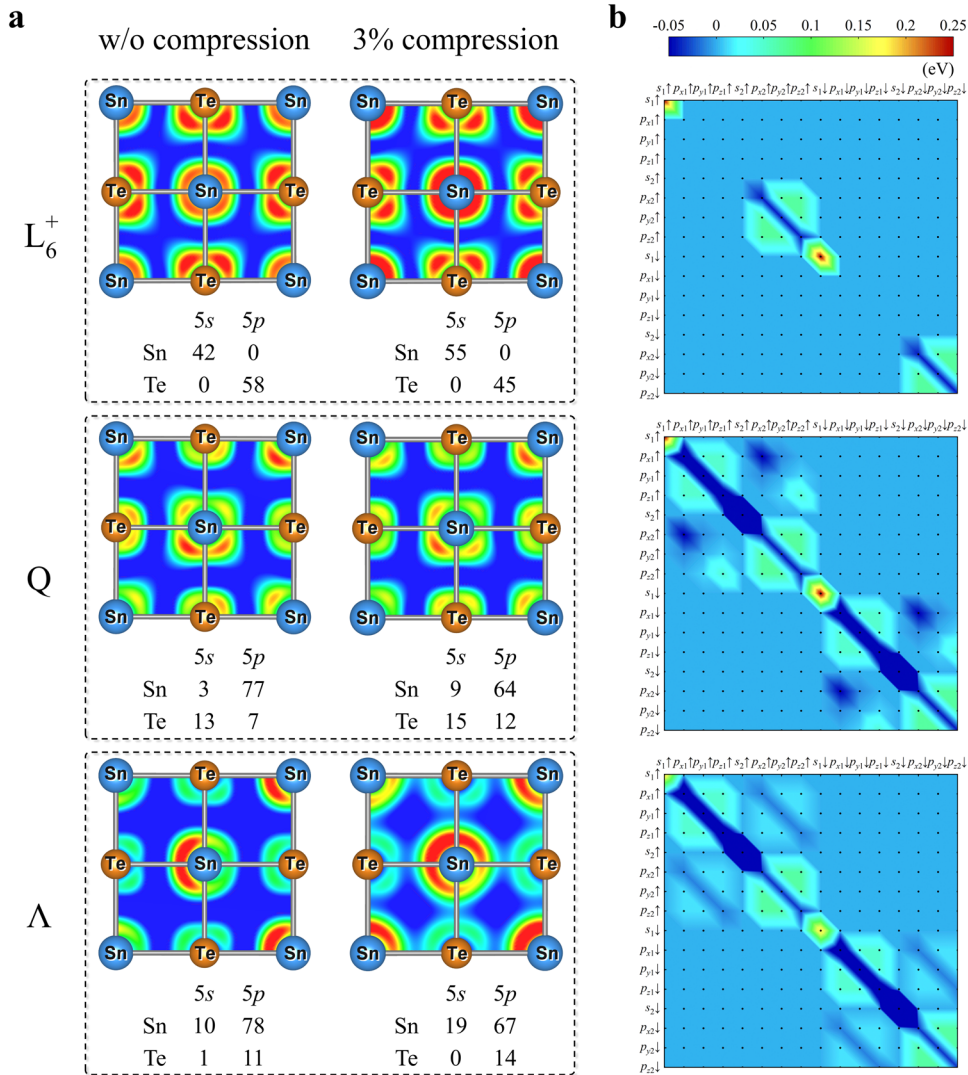


Fig. 2 Orbital contribution to the electron band and tight-binding analysis. **a** The Wave function squares of L_6^+ , Q , and Λ points projected onto the (100) plane of the unstrained and 3% compressed SnTe. The numbers below the corresponding figures show the atomic orbital components in terms of percentages. **b** Differences in matrix elements of Hamiltonian at L_6^+ , Q , and Λ points between the unstrained and 3% compressed SnTe. The blue and red areas represent the decreases and increases of the Hamiltonian, respectively. It should be noted that although the results are expressed with color gradient maps, only the results displayed on the black points are meaningful.

same phenomena happen in Te-5p electrons with different orbital angular momenta. Although the overlapping of the respective $5p_x$, $5p_y$, and $5p_z$ wavefunctions between each two nearest Te are decreased (colored with blue), our calculations of the atomic orbital components indicate that this effect might not be so significant as the mentioned delocalization of the Te-5p orbitals with different angular momenta. Through the tight-binding calculations, these Hamiltonians can be used to reproduce the band structures of SnTe with and without compression (see Supplementary Fig. 3 in the Supplementary Material).

The distinct change of the band structure inevitably changes the electron DOSs and the scattering channels of the electron-phonon (e-ph) interactions, and hence the transport properties. Figure 3 shows the electron scattering rates due to the e-ph interaction of SnTe with different compressive strains. Some interesting results can be observed. The scattering rates near the CBM are initially enhanced and then decrease as the strain increases, which differs from the behavior of the iconic semiconductor, silicon, whose scattering rate and band structure change monotonically with a varying lattice constant (see Supplementary Method 2 and Supplementary Fig. 4 in the

Supplementary Material). Theoretical analysis has elucidated the fact that the profile of the e-ph scattering rate in the low-energy region is mainly determined by the DOS as long as the predominant phonons have small energy, i.e., the long-wavelength acoustic mode⁴⁷. Around the CBM of SnTe, the constant energy surface forms an ellipsoid shape in the Brillouin zone. The surface in the vicinity of the Q point is asymmetrically forming a more oblate ellipsoid as the formation of the double valleys, which is also shown in the previous theoretical study⁴⁸. This feature renders the compressed SnTe the larger electron DOS near the band edge. One can obtain the relation of $\tau_{nk}^{-1} \sim \varepsilon^2$ by assuming that the electron transport is dominated by acoustic-deformation-potential scattering, for which the index of 2 stems from the DOS of a linear band⁴⁹. We show that the CBM of SnTe is sensitive to the strain, and therefore the DOS is correspondingly altered, as plotted with the solid black lines in Fig. 3. It can be seen that the profile of the electron scattering rate is similar to that of the DOS. Therefore, the non-monotonic variation of the scattering rate with the increasing strain can be attributed to the change of the DOS arising from the single- to double-valley transition.

This feature suggests a feasible route to non-monotonically modulating the e-ph scattering channels by applying strain.

The ε^2 trend fails to describe the energy dependence of the electron scattering rate of *n*-type SnTe. Interestingly, the departure of the index from 2 becomes smaller when the compressive strain is applied. The fitted indices of the unstrained, 1% compressed, and 3% compressed SnTe are 0.70, 0.94, and 1.41, respectively. The unstrained crystal shows the largest deviation while it is closer

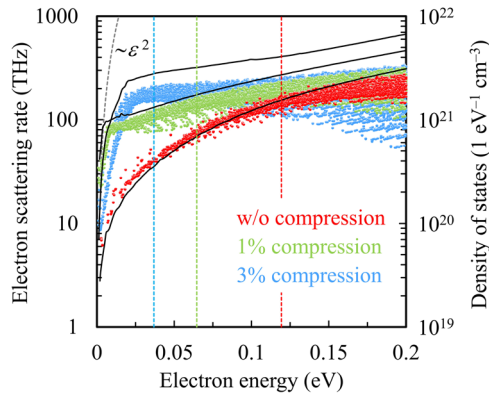


Fig. 3 Ab initio e-ph scattering rates of *n*-type SnTe at 300 K with a doping concentration of 10^{20} cm^{-3} . The red, green, and blue dots represent the crystal at 0%, 1%, and 3% compression, respectively, and the vertical dashed lines with the same colors show the Fermi energies at this doping concentration. The black lines next to the dots are the corresponding electron DOSs. The dashed gray line shows the $\tau_{nk}^{-1} \sim \varepsilon^2$ law of the e-ph scattering rate.

to the typical $\varepsilon^{0.5}$ law given by a parabolic band compared to the compressed crystals. Using the Kane band model, $\varepsilon(1 + \delta\varepsilon) = \hbar^2 |\mathbf{k}|^2 / 2m_{\text{eff}}^{50}$, the fitted effective mass and band non-parabolicity along the $W \rightarrow L \rightarrow \Gamma$ direction are $m_{\text{eff}} = 0.102$ and $\delta = 2.97 \text{ eV}^{-1}$, respectively. The CBM moves from the L to the Q point when the compressive strain increases. The electron scattering rate in the Q valley changes faster with rising energy, which indicates that the band shape becomes more and more linear by increasing compressive strain. As is known, a Kane band with an enormous non-parabolicity factor is asymptotically equivalent to a Dirac band. For the case of the 3% compressed SnTe, the fitted effective mass and band non-parabolicity of the Q valley are, respectively, 0.041 and 27.63 eV^{-1} . On the other hand, the presence of the electron intervalley transition causes the scattering rates to be more dispersive when the electron energy is beyond 0.08 eV, which is the bottom of the Λ valley. This indicates that once the strain-induced intervalley transitions between the first (Q) and second (Λ) valleys are allowed, the e-ph interaction shows stronger momentum dependency. Similar effects can be found in other materials that have a second valley for conducting electrons, such as the high-temperature phase SnSe⁵¹.

Figures 4a and b show the electron scattering rates due to each phonon mode without a strain and with 3% compression, respectively. The Fröhlich phonons, namely, the longitudinal-optical (LO) phonons at the long-wavelength limit, can induce a finite electron scattering rate at the band edge. As the electron energy increases, the total scattering rate is soon taken over by the longitudinal-acoustic phonons. The main reason for this is the fact that the electron scattering arising from acoustic phonons has the trend of scaling as DOS that is high deep in the bands⁴⁷. In addition, the strong dielectric screening in SnTe (the static and

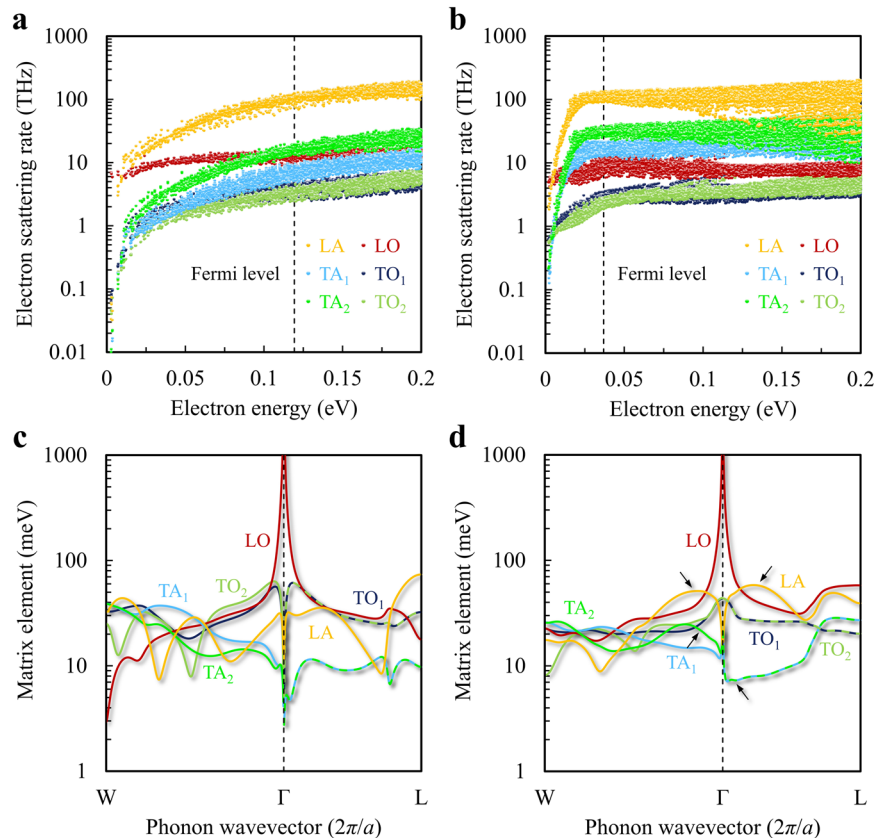


Fig. 4 Ab initio electron scattering rates due to each phonon mode at 300 K with a doping concentration of 10^{20} cm^{-3} . **a** The unstrained and **b** 3% compressed SnTe. The dashed black lines show the Fermi levels. Magnitudes of the coupling matrix elements between an electron at the CBM and the phonons in the ΓW and ΓL directions of the **c** unstrained and **d** 3% compressed SnTe. The black arrows indicate the enhancement in the matrix elements arising from a 3% compressive strain.

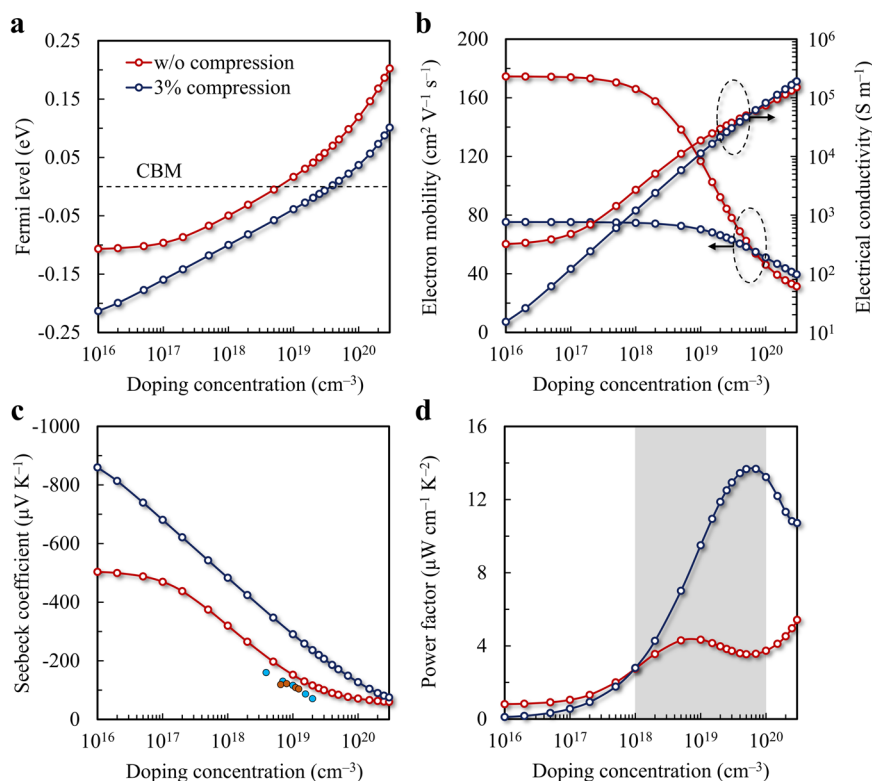


Fig. 5 Thermoelectric transport properties of *n*-type SnTe at 300 K with different doping concentrations. **a** The Fermi level, **b** electron mobility and electrical conductivity, **c** Seebeck coefficient, and **d** power factor of *n*-type SnTe for different doping concentrations at 300 K. The red and blue circles represent the crystal at 0% and 3% compression, respectively. The solid circles in **c** illustrate the experimental results⁴².

high-frequency dielectric coefficients are $\epsilon_s = 1770$ and $\epsilon_\infty = 45$, respectively⁵²) can effectively suppress the phonon-induced dipoles, and consequently, only the atomic vibrations carrying almost opposite phases are strong enough to resist the electron transport near the band edge. One can see the magnitudes of the e-ph matrix elements plotted in Fig. 4c and d. The “cores” induced by the Fröhlich interaction in the vicinity of the Γ point are very narrow compared to those of GaAs, a typically strongly polar semiconductor⁵³. As the strain increases, the scattering rates due to LO phonons do not change significantly in addition to the more dispersive distribution, as previously explained. In contrast, comparing Fig. 4b to a, the scattering rates due to the acoustic phonons near the band edge are enhanced by about one order of magnitude. Figure 4d illustrates the fact that the magnitudes of the matrix elements between the electrons and acoustic phonons with small momentums are increased (emphasized with black arrows), which reflects the fact that in a compressed crystal, the long-wavelength lattice waves give rise to larger disturbances in the potential energy and stronger e-ph interactions in consequence. In general, electron scattering rates should be low when a material is expected to be a good electrical conductor. However, as indicated by the dashed black lines in Fig. 4a and b, the Fermi level of the compressed SnTe is closer to the CBM than that of the unstrained SnTe with the same doping concentration of 10^{20} cm^{-3} . The positions of the Fermi levels with other doping concentrations are plotted in Fig. 5a. This feature, in turn, favors the electrical conduction of high doping concentrations, as discussed below.

Figure 5b shows the ab initio electron mobility and electrical conductivity. The intrinsic mobility of the unstrained SnTe is $174.5 \text{ cm}^2 \text{ V}^{-1} \text{ s}^{-1}$, which is in agreement with the previous model prediction ($\mu \sim 170 \text{ cm}^2 \text{ V}^{-1} \text{ s}^{-1}$ when $n_c < 10^{18} \text{ cm}^{-3}$ ⁴²). Recent measurement results of electron mobility range from 100 to $600 \text{ cm}^2 \text{ V}^{-1} \text{ s}^{-1}$, depending on how many Br or I dopants are introduced into the $\text{Sn}_{0.6}\text{Pb}_{0.4}\text{Te}$ alloys^{42,43}. The electron mobility

decreases to $75.2 \text{ cm}^2 \text{ V}^{-1} \text{ s}^{-1}$ when a 3% compressive strain is applied to the crystal, and the electrical conductivity also shows a significant reduction. The degradation of the electron transport is due to the larger electron-acoustic-phonon scattering near the conduction band edge, as illustrated in Fig. 4b. Surprisingly, with the increasing carrier concentration, both the electron mobility and the electrical conductivity of the two crystals become closer, and then the mobility and the conductivity of the 3% compressed SnTe exceed the values for the unstrained SnTe at the doping concentration of $7 \times 10^{19} \text{ cm}^{-3}$. This is because the presence of the double-valley structure greatly enhances the DOSs near the CBM, which tends to retain the Fermi level in the low-energy region with increasing doping concentration. In the unstrained SnTe, the total scattering rates of the dominant electrons are approximately 100 THz (see red dots and dashed line in Fig. 3). For the case of the compressed SnTe, the Fermi level is only 0.04 eV higher than the CBM, which indicates that the electrons near the CBM whose scattering rates are from 0 to 100 THz (see blue dots and dashed line in Fig. 3) have the probability of contributing to electrical conduction with less resistance. This explains why the compressed SnTe has better electrical performance than the unstrained SnTe at high carrier concentrations.

Figure 5c shows the room-temperature Seebeck coefficients with different doping concentrations. The calculated Seebeck coefficients are inversely proportional to the carrier density, which is in accordance with the prediction of the Pisarenko relation⁴². At low doping concentrations, the compressed SnTe has the higher Seebeck coefficient because of its larger electron DOS (as shown in the solid black lines in Fig. 3) due to the double-valley structure. At high doping concentrations, since the Fermi level is inside the conduction band, an electron can yield either a positive or negative Seebeck coefficient depending on its relative energy with respect to the position of the Fermi level. A large electron DOS near the CBM imposes the encumbrance of

the thermoelectric conversion rate since more electrons are providing the positive Seebeck coefficient. Fortunately, the double-valley band structure also prevents the Fermi level from going deep inside the conduction band. As previously mentioned, for the case of the compressed SnTe at the doping concentration of 10^{20} cm^{-3} , the Fermi level is located approximately at the center between the Q and Λ points. Therefore, even at such a high doping concentration, the Seebeck coefficient of the compressed SnTe ($-127.2 \mu\text{V K}^{-1}$) is still roughly about double that of the unstrained SnTe ($-71.7 \mu\text{V K}^{-1}$). As a result, the simultaneously enhanced electrical conductivity and the Seebeck coefficient lead to a remarkable increase in the power factor of the doping concentrations from 10^{18} to 10^{20} cm^{-3} , which is of great interest in thermoelectric applications, as shown by the shaded region in Fig. 5d. In our calculations, the largest power factor of the compressed SnTe ($13.7 \mu\text{W cm}^{-1} \text{ K}^{-2}$) occurs at the doping concentration of $5 \times 10^{19} \text{ cm}^{-3}$, and this power factor is 3.9 times larger than that of the unstrained SnTe ($3.5 \mu\text{W cm}^{-1} \text{ K}^{-2}$).

In summary, we theoretically examined the room-temperature electron transport properties of *n*-type SnTe with different compressive strains and doping concentrations. The compressive strain induced a single- to double-valley transition in the lowest conduction band. The tight-binding analysis demonstrated that the variation of the band shape originated from the strain-induced delocalization of both the Sn-5s electrons and the Te-5p electrons with different orbital angular momenta. The ab initio calculations show that the 3% compressed SnTe has a larger electrical conductivity and Seebeck coefficient than those of the unstrained SnTe at high doping concentrations. In the region of doping concentration from 10^{19} to 10^{20} cm^{-3} , the thermoelectric power factor can be significantly improved up to 3.9 times by a 3% compression, and the peak value occurs at the doping concentration of $5 \times 10^{19} \text{ cm}^{-3}$. The main cause leading to the enhancement is the presence of the strain-induced double-valley band structure. The increasing electron DOS directly contributes to the Seebeck coefficient. It also tends to retain the position of the Fermi level close to the CBM as the doping level increases, which benefits the electrical conductivity due to the much lower e-ph scattering rates around the band edge. Very recently, *n*-type SnTe has proven to be a good candidate for thermoelectric material. Our results further revealed the origin of the single- to double-valley transition of the Dirac-like band, and provided the theoretical basis for understanding the enhancement of the power factor in *n*-type SnTe with strain engineering. Additionally, the results presented a possible degree of freedom for manipulating the thermoelectric properties of semiconductors possessing Dirac-like bands.

METHODS

Ab initio calculations

The e-ph coupling matrix elements should be determined to study the electron scattering rates and transport properties. At finite temperature, a traveling electron can interact with the variation of the crystal potential due to atomic vibrations, and the process is known as the e-ph scattering. The matrix elements are used to describe the scattering events that fulfill energy and momentum conservation, which are given by⁵⁴

$$\mathbf{M}_{nk, pq}^{mk+q} = \left(\frac{\hbar}{2m_0\omega_{pq}} \right)^{1/2} \langle m\mathbf{k} + \mathbf{q} | \delta V_{pq}(\mathbf{r}) | n\mathbf{k} \rangle. \quad (1)$$

In the expression, $n\mathbf{k}$ and $p\mathbf{q}$ denote the band index and the momenta for electrons and phonons, respectively; m_0 is a reference mass, and ω_{pq} is the phonon frequency. The operator $\delta V_{pq}(\mathbf{r})$ is the variation of the self-consistent potential energy caused by a lattice wave corresponding to a phonon with the

state $p\mathbf{q}$ (sometimes called the phonon perturbed potential). Using Fermi's golden rule and the relaxation time approximation, the scattering rate of an electron with the state $n\mathbf{k}$ due to the e-ph interaction is written as⁵⁴

$$\frac{1}{\tau_{nk}} = \frac{2\pi}{\hbar} \sum_{m,p} \int_{\Omega_{BZ}} \frac{d\mathbf{q}}{\Omega_{BZ}} |\mathbf{M}_{nk, pq}^{mk+q}|^2 \left[\frac{(f_{mk+q} + n_{pq})\delta(\varepsilon_{nk} - \varepsilon_{mk+q} + \hbar\omega_{pq})}{(1 - f_{mk+q} + n_{pq})\delta(\varepsilon_{nk} - \varepsilon_{mk+q} - \hbar\omega_{pq})} \right], \quad (2)$$

where Ω_{BZ} is the volume of the first Brillouin zone, ε_{nk} is the electron energy, and f_{nk} and n_{pq} are the Fermi-Dirac and Bose-Einstein distribution functions, respectively. The first term in the bracket represents the phase space of a phonon-absorption scattering event, and the second term is for the phonon-emission scattering event. With the scattering rates, the tensors of the electrical conductivity and the Seebeck coefficient are, respectively, calculated with

$$\sigma_{\alpha\beta} = \frac{e^2}{\Omega N_{\mathbf{k}}} \sum_{n\mathbf{k}} v_{n\mathbf{k},\alpha} v_{n\mathbf{k},\beta} \tau_{nk} \frac{\partial f_{nk}}{\partial \varepsilon_{nk}}, \quad (3)$$

$$S_{\alpha\beta} = -\frac{1}{eT} \left[\sum_{n\mathbf{k}} v_{n\mathbf{k},\alpha} v_{n\mathbf{k},\beta} \tau_{nk} \frac{\partial f_{nk}}{\partial \varepsilon_{nk}} \right]^{-1} \sum_{n\mathbf{k}} (\varepsilon_{nk} - \varepsilon_F) v_{n\mathbf{k},\alpha} v_{n\mathbf{k},\beta} \tau_{nk} \frac{\partial f_{nk}}{\partial \varepsilon_{nk}}, \quad (4)$$

where Ω is the volume of the studied crystal cell, $N_{\mathbf{k}}$ is the number of grid points in the \mathbf{k} -mesh, ε_F is the Fermi energy, and $v_{n\mathbf{k},\alpha}$ is the α component of the electron group velocity. The electron mobility tensor at a given carrier concentration, n_c , is calculated with $\mu_{\alpha\beta} = (en_c)^{-1} \sigma_{\alpha\beta}$.

The electron and phonon band structures are studied by DFT using the Quantum ESPRESSO package⁵⁵. A fully relativistic norm-conserving pseudopotential with Becke-Perdew exchange-correlation functional including generalized gradient approximation is used in this study. The self-consistent field calculations are performed on a $20 \times 20 \times 20$ \mathbf{k} -mesh, and the electronic Hamiltonians and energies are extracted from a $12 \times 12 \times 12$ \mathbf{k} -mesh after carrying out the non-self-consistent field calculations. The cutoff energy of the plane wave is 90 Ry, and the convergence threshold is set to be 10^{-12} Ry. The optimized cell parameter is $a_{\text{opt}} = 6.410 \text{ \AA}$, which is in good agreement with previous study⁵⁶ but is larger than the experimental value ($a_{\text{exp}} = 6.327 \text{ \AA}$ ⁵⁷). The calculated bandgap is 0.086 eV, and we shift the gap to the experimental value (0.180 eV⁵⁸) using rigid band approximation to obtain a more precisely determined Fermi level. The phonon perturbed potentials are computed on a $6 \times 6 \times 6$ \mathbf{q} -mesh using a convergence threshold of 10^{-19} Ry. It should be noted that in the calculations below, the dynamical matrices are replaced by the results calculated using a pseudopotential with the Perdew-Zunger exchange-correlation functional, including the local density approximation because this can provide a more accurate phonon band, as discussed in a previous study³⁰. Our in-house modified EPW package⁵⁹ is employed to calculate the e-ph scattering rates on a $200 \times 200 \times 200$ \mathbf{k} -mesh and the electron transport properties at 300 K with different doping concentrations and compressive strains. The delta functions in Eq. (2) are computed using the parameter-free tetrahedron technique⁶⁰. The scattering rate of each electron eigenstate is calculated by interacting with the phonon eigenstates on a $100 \times 100 \times 100$ \mathbf{q} -mesh.

Tight-binding analysis

The band energies can be computed by diagonalizing the electronic Hamiltonians associated with a given crystal structure.

The full Hamiltonian matrix including the SOC is written as

$$\mathbf{H}(\mathbf{k}) = \begin{bmatrix} \mathbf{h}_{aa}^0(\mathbf{k}) + \mathbf{h}_a^{\text{SO}}(\uparrow\uparrow) & \mathbf{h}_{ac}^0(\mathbf{k}) & \mathbf{h}_a^{\text{SO}}(\uparrow\downarrow) & \mathbf{0} \\ \mathbf{h}_{ca}^0(\mathbf{k}) & \mathbf{h}_{cc}^0(\mathbf{k}) + \mathbf{h}_c^{\text{SO}}(\uparrow\uparrow) & \mathbf{0} & \mathbf{h}_c^{\text{SO}}(\uparrow\downarrow) \\ \mathbf{h}_a^{\text{SO}}(\downarrow\uparrow) & \mathbf{0} & \mathbf{h}_{aa}^0(\mathbf{k}) + \mathbf{h}_a^{\text{SO}}(\downarrow\downarrow) & \mathbf{h}_{ac}^0(\mathbf{k}) \\ \mathbf{0} & \mathbf{h}_c^{\text{SO}}(\downarrow\uparrow) & \mathbf{h}_{ca}^0(\mathbf{k}) & \mathbf{h}_{cc}^0(\mathbf{k}) + \mathbf{h}_c^{\text{SO}}(\downarrow\downarrow) \end{bmatrix}, \quad (5)$$

where the subscripts a and c represent the cation (Sn) and anion (Te in this study), respectively, the superscripts '0' and 'SO' denote the component of the unperturbed crystal Hamiltonian, \mathbf{h}^0 , and the SOC Hamiltonian, \mathbf{h}^{SO} , respectively, and the arrows indicate the spin polarization. Each element in Eq. (5) corresponds to a 4 × 4 matrix. For example, the elements including the SOC have

$$\mathbf{h}_v^{\text{SO}}(\uparrow\uparrow) = [\mathbf{h}_v^{\text{SO}}(\downarrow\downarrow)]^* = \begin{bmatrix} 0 & 0 & 0 & 0 \\ 0 & 0 & -i\lambda_v & 0 \\ 0 & i\lambda_v & 0 & 0 \\ 0 & 0 & 0 & 0 \end{bmatrix}, \quad (6)$$

$$\mathbf{h}_v^{\text{SO}}(\uparrow\downarrow) = [\mathbf{h}_v^{\text{SO}}(\downarrow\uparrow)]^\dagger = \begin{bmatrix} 0 & 0 & 0 & 0 \\ 0 & 0 & 0 & \lambda_v \\ 0 & 0 & 0 & -i\lambda_v \\ 0 & -\lambda_v & i\lambda_v & 0 \end{bmatrix}, \quad (7)$$

where v can be a or c . λ_v reflects the strength of the SOC in the band structure. The processes of fitting the Slater-Koster parameters are performed on the TBFIT code⁶¹. See Supplementary Method 1 for the details of the tight-binding calculations.

DATA AVAILABILITY

The data that supports this work can be found in the Manuscript and Supplemental Material. Additional data will be available from the corresponding author upon reasonable request.

Received: 14 July 2022; Accepted: 1 November 2022;

Published online: 12 November 2022

REFERENCES

- DiSalvo, F. J. Thermoelectric cooling and power generation. *Science* **285**, 703–706 (1999).
- Venkatasubramanian, R., Siivola, E., Colpitts, T. & O'Quinn, B. Thin-film thermoelectric devices with high room-temperature figures of merit. *Nature* **413**, 597–602 (2001).
- Mao, J. et al. High thermoelectric cooling performance of n -type Mg_3Bi_2 -based materials. *Science* **365**, 495–498 (2019).
- Qin, B. et al. Power generation and thermoelectric cooling enabled by momentum and energy multiband alignments. *Science* **373**, 556–561 (2021).
- Poudel, B. et al. High-thermoelectric performance of nanostructured bismuth antimony telluride bulk alloys. *Science* **320**, 634–638 (2008).
- Mao, J., Chen, G. & Ren, Z. Thermoelectric cooling materials. *Nat. Mater.* **20**, 454–461 (2021).
- Liu, Z. et al. Maximizing the performance of n -type Mg_3Bi_2 based materials for room-temperature power generation and thermoelectric cooling. *Nat. Commun.* **13**, 1120 (2022).
- Snyder, G. J. & Toberer, E. S. Complex thermoelectric materials. *Nat. Mater.* **7**, 105–114 (2008).
- Zhu, G. et al. Increased phonon scattering by nanograins and point defects in nanostructured silicon with a low concentration of germanium. *Phys. Rev. Lett.* **102**, 196803 (2009).
- Guin, S. N., Negi, D. S., Datta, R. & Biswas, K. Nanostructuring, carrier engineering and bond anharmonicity synergistically boost the thermoelectric performance of p -type $\text{AgSbSe}_2\text{-ZnSe}$. *J. Mater. Chem. A* **2**, 4324–4331 (2014).
- Hochbaum, A. I. et al. Enhanced thermoelectric performance of rough silicon nanowires. *Nature* **451**, 163–167 (2008).
- Biswas, K. et al. High-performance bulk thermoelectrics with all-scale hierarchical architectures. *Nature* **489**, 414–418 (2012).

- Zhao, L.-D. et al. All-scale hierarchical thermoelectrics: MgTe in PbTe facilitates valence band convergence and suppresses bipolar thermal transport for high performance. *Energy Environ. Sci.* **6**, 3346–3355 (2013).
- Pei, Y. et al. Convergence of electronic bands for high performance bulk thermoelectrics. *Nature* **473**, 66–69 (2011).
- Tang, Y. et al. Convergence of multi-valley bands as the electronic origin of high thermoelectric performance in CoSb_3 skutterudites. *Nat. Mater.* **14**, 1223–1228 (2015).
- Heremans, J. P. et al. Enhancement of thermoelectric efficiency in PbTe by distortion of the electronic density of states. *Science* **321**, 554–557 (2008).
- Zhang, Q. et al. High thermoelectric performance by resonant dopant indium in nanostructured SnTe. *Proc. Natl Acad. Sci. U. S. A.* **110**, 13261–13266 (2013).
- May, A. F., Fleurial, J.-P. & Snyder, G. J. Thermoelectric performance of lanthanum telluride produced via mechanical alloying. *Phys. Rev. B* **78**, 125205 (2008).
- Li, J., Zhang, X., Lin, S., Chen, Z. & Pei, Y. Realizing the high thermoelectric performance of GeTe by Sb-doping and Se-alloying. *Chem. Mater.* **29**, 605–611 (2017).
- Li, Y. et al. Enhancing thermoelectric properties of monolayer GeSe via strain engineering: A first principles study. *Appl. Surf. Sci.* **521**, 146256 (2020).
- He, J. & Tritt, T. M. Advances in thermoelectric materials research: Looking back and moving forward. *Science* **357**, eaak9997 (2017).
- Moshwan, R., Yang, L., Zou, J. & Chen, Z.-G. Eco-friendly SnTe thermoelectric materials: progress and future challenges. *Adv. Funct. Mater.* **27**, 1703278 (2017).
- Chen, Z. et al. Routes for advancing SnTe thermoelectrics. *J. Mater. Chem. A* **8**, 16790–16813 (2020).
- Hsieh, T. H. et al. Topological crystalline insulators in the SnTe material class. *Nat. Commun.* **3**, 982 (2012).
- Tanaka, Y. et al. Experimental realization of a topological crystalline insulator in SnTe. *Nat. Phys.* **8**, 800–803 (2012).
- Ye, Z.-Y. et al. The origin of electronic band structure anomaly in topological crystalline insulator group-IV tellurides. *NPJ Comput. Mater.* **1**, 15001 (2015).
- Qian, X., Fu, L. & Li, J. Topological crystalline insulator nanomembrane with strain-tunable band gap. *Nano Res* **8**, 967–979 (2015).
- Zhou, D., Li, D., Ma, Y., Cui, Q. & Chen, C. Pressure-driven enhancement of topological insulating state in tin telluride. *J. Phys. Chem. C* **117**, 8437–8442 (2013).
- Xie, G. et al. Band inversion induced multiple electronic valleys for high thermoelectric performance of SnTe with strong lattice softening. *Nano Energy* **69**, 104395 (2020).
- Liu, T.-H. et al. Electron mean-free-path filtering in Dirac material for improved thermoelectric performance. *Proc. Natl Acad. Sci. U. S. A.* **115**, 879–884 (2018).
- Tan, X. et al. Band engineering and improved thermoelectric performance in M-doped SnTe (M = Mg, Mn, Cd, and Hg). *Phys. Chem. Chem. Phys.* **18**, 7141–7147 (2016).
- He, J. et al. Valence band engineering and thermoelectric performance optimization in SnTe by Mn-alloying via a zone-melting method. *J. Mater. Chem. A* **3**, 19974–19979 (2015).
- Tan, G. et al. Extraordinary role of Hg in enhancing the thermoelectric performance of p -type SnTe. *Energy Environ. Sci.* **8**, 267–277 (2015).
- Al Rahal Al Orabi, R. et al. Band degeneracy, low Thermal conductivity, and high thermoelectric figure of merit in SnTe-CaTe alloys. *Chem. Mater.* **28**, 376–384 (2016).
- Zhang, L. et al. Enhanced thermoelectric performance through synergy of resonance levels and valence band convergence via Q/In (Q = Mg, Ag, Bi) co-doping. *J. Mater. Chem. A* **6**, 2507–2516 (2018).
- Shenoy, U. S. & Bhat, D. K. Bi and Zn co-doped SnTe thermoelectrics: interplay of resonance levels and heavy hole band dominance leading to enhanced performance and a record high room temperature ZT. *J. Mater. Chem. C* **8**, 2036–2042 (2020).
- Hussain, T. et al. Realizing high thermoelectric performance in eco-friendly SnTe via synergistic resonance levels, band convergence and endotaxial nanostructuring with Cu_2Te . *Nano Energy* **73**, 104832 (2020).
- Zhao, L.-D. et al. Enhanced thermoelectric properties in the counter-doped SnTe system with strained endotaxial SrTe. *J. Am. Chem. Soc.* **138**, 2366–2373 (2016).
- Min, Y. et al. Vacancy engineering in rock-salt type (IV-VI)_x(V-VI) materials for high thermoelectric performance. *Nano Energy* **78**, 105198 (2020).
- Acharya, S., Pandey, J. & Soni, A. Soft phonon modes driven reduced thermal conductivity in self-compensated $\text{Sn}_{1.03}\text{Te}$ with Mn doping. *Appl. Phys. Lett.* **109**, 133904 (2016).
- Xu, L., Wang, H.-Q. & Zheng, J.-C. Thermoelectric properties of PbTe, SnTe, and GeTe at high pressure: an ab initio study. *J. Electron. Mater.* **40**, 641–647 (2011).
- Pang, H. et al. Realizing n -type SnTe thermoelectrics with competitive performance through suppressing Sn vacancies. *J. Am. Chem. Soc.* **143**, 8538–8542 (2021).
- Guo, C., Wang, D., Zhang, X. & Zhao, L.-D. One–one correspondence between n -type SnTe thermoelectric and topological phase transition. *Chem. Mater.* **34**, 3423–3429 (2022).

44. Drüppel, M., Krüger, P. & Rohlfing, M. Strain tuning of Dirac states at the SnTe (001) surface. *Phys. Rev. B* **90**, 155312 (2014).
45. Chattopadhyay, T., Boucherle, J. X. & Schnering, H. G. Neutron diffraction study on the structural phase transition in GeTe. *J. Phys. C: Solid State Phys.* **20**, 1431–1440 (1987).
46. Gallo, C. F., Miller, R. C., Sutter, P. H. & Ure, R. W. Jr Bipolar electronic thermal conductivity in semimetals. *J. Appl. Phys.* **33**, 3144 (1962).
47. Lundstrom, M. *Fundamentals of carrier transport* (Cambridge Uni. Press, Cambridge, 2009).
48. Chen, X., Parker, D. & Singh, D. J. Importance of non-parabolic band effects in the thermoelectric properties of semiconductors. *Sci. Rep.* **3**, 3168 (2013).
49. Watzman, S. J. et al. Dirac dispersion generates unusually large Nernst effect in Weyl semimetals. *Phys. Rev. B* **97**, 161404(R) (2018).
50. Kane, E. O. Band structure of indium antimonide. *J. Phys. Chem. Solids* **1**, 249–261 (1957).
51. Zhou, W., Dai, Y., Liu, T.-H. & Yang, R. Effects of electron-phonon intervalley scattering and band nonparabolicity on electron transport properties of high-temperature phase SnSe: An ab initio study. *Mater. Today Phys.* **22**, 100592 (2022).
52. Burstein, E., Perkowitz, S. & Brodsky, M. H. The dielectric properties of the cubic IV-VI compound semiconductors. *J. Phys. Colloq.* **29**, C4-78–C4-83 (1968).
53. Liu, T.-H., Zhou, J., Liao, B., Singh, D. J. & Chen, G. First-principles mode-by-mode analysis for electron-phonon scattering channels and mean free path spectra in GaAs. *Phys. Rev. B* **95**, 075206 (2017).
54. Ziman, J. M. *Electrons and Phonons: The Theory of Transport Phenomena in Solids* (Clarendon Press, Oxford, 1960).
55. Giannozzi, P. et al. QUANTUM ESPRESSO: a modular and open-source software project for quantum simulations of materials. *J. Phys.: Condens. Matter* **21**, 395502 (2009).
56. Wang, N. et al. Microscopic origin of the *p*-type conductivity of the topological crystalline insulator SnTe and the effect of Pb alloying. *Phys. Rev. B* **89**, 045142 (2014).
57. Brebrick, R. F. Composition stability limits for the rocksalt-structure phase $(\text{Pb}_{1-x}\text{Sn}_x)_{1-x}\text{Te}_x$ from lattice parameter measurements. *J. Phys. Chem. Solids* **32**, 551–562 (1971).
58. Rogers, L. M. Valence band structure of SnTe. *J. Phys. D: Appl. Phys.* **1**, 845–852 (1968).
59. Poncé, S., Margine, E. R., Verdi, C. & Giustino, F. EPW: Electron-phonon coupling, transport and superconducting properties using maximally localized Wannier functions. *Comput. Phys. Commun.* **209**, 116–133 (2016).
60. Lambin, P. & Vigneron, J. P. Computation of crystal Green's functions in the complex-energy plane with the use of the analytical tetrahedron method. *Phys. Rev. B* **29**, 3430 (1984).
61. Kim, H.-J. TBFIT, <https://github.com/Infant83/TBFIT>.

ACKNOWLEDGEMENTS

Y.D. and W.Z. contributed equally to this work. T.-H.L. and R.Y. acknowledge that this work was financially supported from the National Key Research and Development Program of China under Grant No. 2022YFB3803900 and from the National Natural

Science Foundation of China under Grant No. 52076089. H.-J.K. gratefully acknowledges financial support from the AIDAS project of the Forschungszentrum Jülich and CEA and from the Alexander von Humboldt Foundation (No. KOR 1211335 HFST-P). The computation is completed in the HPC Platform of Huazhong University of Science and Technology.

AUTHOR CONTRIBUTIONS

Y.D., W.Z., T.-H.L., and X.Q. carried out the ab initio calculations; Y.D., H.-J.K., and Q.S. performed the tight-binding calculations; Y.D., T.-H.L. and R.Y. wrote the manuscript; T.-H.L. and R.Y. supervised the research; All of the authors discussed the results and edited the manuscript.

COMPETING INTERESTS

The authors declare no competing interests.

ADDITIONAL INFORMATION

Supplementary information The online version contains supplementary material available at <https://doi.org/10.1038/s41524-022-00927-z>.

Correspondence and requests for materials should be addressed to Te-Huan Liu or Ronggui Yang.

Reprints and permission information is available at <http://www.nature.com/reprints>

Publisher's note Springer Nature remains neutral with regard to jurisdictional claims in published maps and institutional affiliations.



Open Access This article is licensed under a Creative Commons Attribution 4.0 International License, which permits use, sharing, adaptation, distribution and reproduction in any medium or format, as long as you give appropriate credit to the original author(s) and the source, provide a link to the Creative Commons license, and indicate if changes were made. The images or other third party material in this article are included in the article's Creative Commons license, unless indicated otherwise in a credit line to the material. If material is not included in the article's Creative Commons license and your intended use is not permitted by statutory regulation or exceeds the permitted use, you will need to obtain permission directly from the copyright holder. To view a copy of this license, visit <http://creativecommons.org/licenses/by/4.0/>.

© The Author(s) 2022